Kauppinen, S.; Karhula, S. S.; Thevenot, J.; Ylitalo, Tuomo; Rieppo, L.; Kestilä, I.; Haapea, M.; Hadjab, I.; Finnilä, M. A.; Quenneville, E.; Garon, M.; Gahunia, H. K.; Pritzker, K. P.H.; Buschmann, M. D.; Nieminen, H. J.

3D morphometric analysis of calcified cartilage properties using micro-computed tomography

3D morphometric analysis of calcified cartilage properties using micro-computed tomography

S. Kauppinen † *, S.S. Karhula † ‡, J. Thevenot † ‡, T. Ylitalo §, L. Rieppo †, I. Kestilä †,
M. Haapea † §§, I. Hadjab ‖ ¶, M.A. Finnilä † #, E. Quenneville ¶, M. Garon ¶, H.K. Gahunia ††,
K.P.H. Pritzker †† ‡‡, M.D. Buschmann ‖, S. Saarakkala † §§, H.J. Nieminen † § †† ‖‖

† Research Unit of Medical Imaging, Physics and Technology, University of Oulu, Oulu, Finland
‡ Infotech, University of Oulu, Finland
§ Department of Physics, University of Helsinki, Helsinki, Finland
‖ Polytechnique Montreal, Montreal, Quebec, Canada
¶ Biomomentum Inc., 970 Michelin St., Suite 200, Laval, Quebec H7L 5C1, Canada
# Department of Applied Physics, University of Eastern Finland, Kuopio, Finland
†† Department of Laboratory Medicine and Pathobiology, University of Toronto, Toronto, ON, Canada
‡‡ Department of Laboratory Medicine and Pathobiology, Mount Sinai Hospital, Toronto, ON, Canada
§§ Department of Diagnostic Radiology, Oulu University Hospital, Oulu, Finland
‖‖ Department of Neuroscience and Biomedical Engineering, Aalto University, Espoo, Finland

ARTICLE INFO

SUMMARY

Objective: Our aim is to establish methods for quantifying morphometric properties of calcified cartilage (CC) from micro-computed tomography (μCT). Furthermore, we evaluated the feasibility of these methods in investigating relationships between osteoarthritis (OA), tidemark surface morphology and open subchondral channels (OSCCs).

Method: Samples ($n = 15$) used in this study were harvested from human lateral tibial plateau ($n = 8$). Conventional roughness and parameters assessing local 3-dimensional (3D) surface variations were used to quantify the surface morphology of the CC. Subchondral channel properties (percentage, density, size) were also calculated. As a reference, histological sections were evaluated using Histopathological osteoarthritis grading (OARSI) and thickness of CC and subchondral bone (SCB) was quantified.

Results: OARSI grade correlated with a decrease in local 3D variations of the tidemark surface (amount of different surface patterns ($r_s = -0.600$, $P = 0.018$), entropy of patterns (EP) ($r_s = -0.648$, $P = 0.018$), homogeneity index (HI) ($r_s = 0.555$, $P = 0.032$)) and tidemark roughness (TMR) ($r_s = -0.579$, $P = 0.024$). Amount of different patterns (ADP) and EP associated with channel area fraction (CAF) ($r_p = 0.876$, $P < 0.0001$; $r_p = 0.665$, $P = 0.007$, respectively) and channel density (CD) ($r_p = 0.680$, $P = 0.011$; $r_p = 0.582$, $P = 0.023$, respectively). TMR was associated with CAF ($r_p = 0.926$, $P < 0.0001$) and average channel size ($r_p = 0.574$, $P = 0.025$). CC topography differed statistically significantly in early OA vs healthy samples.

Conclusion: We introduced a μ-CT image method to quantify 3D CC topography and perforations through CC. CC topography was associated with OARSI grade and OSCC properties; this suggests that the established methods can detect topographical changes in tidemark and CC perforations associated with OA.

* Address correspondence and reprint requests to: S. Kauppinen, Research Unit of Medical Imaging, Physics and Technology, University of Oulu, POB 5000, FI-90014 Oulu, Finland. Tel: 358-40-8332405.

E-mail addresses: sami.kauppinen@oulu.fi (S. Kauppinen), sakari.karhula@oulu.fi (S.S. Karhula), jerome.thevenot@oulu.fi (J. Thevenot), tuomo.ylitalo@helsinki.fi (T. Ylitalo), lassi.rieppo@oulu.fi (L. Rieppo), iida.kestila@oulu.fi (I. Kestilä), marianne.haapea@oulu.fi (M. Haapea), insaf.hadjab@polymtl.ca (I. Hadjab), mikko.finnila@oulu.fi (M.A. Finnilä), quenneville@biomomentum.com (E. Quenneville), garon@biomomentum.com (M. Garon), pvgahunia@hotmail.com (H.K. Gahunia), kenpritzker@gmail.com (K.P.H. Pritzker), michael.buschmann@polymtl.ca (M.D. Buschmann), simo.saarakkala@oulu.fi (S. Saarakkala), heikki.j.nieminen@aalto.fi (H.J. Nieminen).

Introduction

Osteoarthritis (OA) is typically considered as a progressive joint disease that produces several pathological changes, such as cartilage matrix erosion, tidemark duplication, bone sclerosis and osteophyte formation[1,2]. However, the pathogenesis of these features is still poorly understood. Many hypotheses have been introduced about the pathogenesis of OA, and some studies focus more on the changes in cartilage matrix and chondrocytes as the source of disease progression[3–6], while some focus on the subchondral bone (SCB) as the main site of OA initiation[7–9]. However, there is evidence that in OA, the morphological changes in periarticular bone predate the changes in articular cartilage[10,11]. This promotes the importance of studying mineralized regions such as calcified cartilage (CC) and SCB. Furthermore, current understanding of OA has also led to the phenotype theory, where initiation site, pathogenesis and underlying other diseases differ, and, therefore, lead to different manifestations of OA.[12]

Noncalcified cartilage (NCC) and SCB are commonly separated by a layer of CC. This layer is important as morphological changes in it can affect the crosstalk[13], biomechanical force distribution[14] and solute transportation[15,16] between the NCC and SCB. The transition boundary from NCC to CC is called tidemark[17], where collagen fibrils of NCC are anchored to the CC[18]. The tidemark is metabolically active structure, representing the calcification front where the NCC becomes the CC possibly associated with matrix vesicles released from the surfaces of deep chondrocytes[19,20]. This process is inhibited by proteoglycans[21] and matrix Gla protein (K-vitamin dependent protein that binds free calcium ions)[22]. Therefore, there is at least some form of metabolical homeostasis in normal tidemark, which is disrupted in OA.

During the progression of OA, the tidemark advances into the NCC, slowly shifting towards superficial cartilage, but typically not exceeding the deep zone cartilage[23]. This is known as tidemark duplication, i.e., more than one tidemark may be present. Simultaneously, the CC is replaced by bone via chondroclastic resorption[24] leading to endochondral ossification[25]. Furthermore, hypocellularity and the presence of hypertrophic chondrocytes are linked to OA progression indicating a diminished number of chondrocytes in OA cartilage[26]. It has also been hypothesized that OA hypertrophic chondrocytes do not inhibit calcification, but act in the same manner as hypertrophic chondrocytes in endochondral ossification leading to degradation of the surrounding extracellular matrix[3]. In previous literature, chondrocytes located at the tidemark can be seen as dimples in scanning electron microscopy (SEM) images[27]. As the chondrocyte size and number affect CC topography and metabolic homeostasis in the tidemark is disrupted in OA, the CC surface topography would be expected to be changed with disease progression.

The CC contains vascular and avascular channels[28]. The subchondral plate, consisting of CC and SCB[29], has three types of channels: (1) open channels encapsulated by CC, (2) closed channels encapsulated by bone and (3) open channels, which reach and penetrate the tidemark[28]. The latter ones are of special interest since they are open channels for nutrition and fluid exchange. The avascular channels can contain soft tissues e.g., adipocytes and bone marrow[28]. Thus, distinguishing avascular from vascular channels with micro-computed tomography (μCT) would require a specific contrast agent to differentiate between vascular tissue from other soft tissues. In this study, we use μCT without contrast agent and therefore we refer to these channels as open subchondral channels (OSCC).

To date, most studies investigating the tidemark or channels through the calcified layer are done from 5 mm thick histological sections[13,30,31]. For instance, studies have been conducted to assess how the tidemark roughness (TMR) is altered as a function of OA[30,31]. Roughness of a 2D surface can be easily calculated as a ratio between the true length of the surface and the projected length of that surface, where the minimum value of one defines a perfectly smooth surface[32]. Vessels in CC are also often studied from histological sections[33–35]. Using histological sections for quantifying CC morphometrics is prone to poor or irregular staining and cutting artifacts, and consequently often requires manual segmentation. A complex 3D structure can be derived from stacked sections of a volume, but the workload of serial sectioning is high and the co-registration of the consecutive histological slices is limited by the sectioning artifacts.

The μCT provides volumetric imaging of tissue blocks, thus overcoming the limitations of conventional histology. High resolution μCT imaging and user-independent segmentation of the tidemark could potentially capture the smallest variations in the tidemark and also the calcified content accurately; importantly, this could be achieved in 3D. Therefore, a μCT approach with software algorithms has the potential to quantify the true TMR with minimal operator input and bias. However, 3D methods to quantify the OA related changes in CC topography and vessel perforations are limited. Therefore, this study aims to establish a μCT based method to quantify the CC topography and OSCC perforations through CC in 3D. Furthermore, we demonstrate that the methods can be used to investigate the relations between OA, tidemark surface roughness and OSCCs.

Materials and methods

Sample preparation and μCT imaging

Samples were harvested from both knees of six patients (age 49–67) (Maisonneuve-Rosemont Hospital, Montreal, Canada) undergoing total knee replacement (TKR) surgery and two asymptomatic cadavers (age 26 and 49) donated by RTI Surgical tissue bank (FL, USA), resulting in 16 tibial plateaus. Osteochondral cores ($n = 15$, $\varnothing = 4$ mm) were drilled from the weight bearing area of lateral tibial plateaus. One sample was excluded as calcified tissue was missing from the lateral weight bearing area. Samples were fixed in buffered 4% formaldehyde and imaged in the fixation media after minimum of 3 days of fixation. Imaging was conducted with the desktop μCT (Skyscan 1272, Brüker microCT, Kontich, Belgium). The following settings were used for projection image acquisition: X-ray tube voltage = 50 kV, X-ray tube current = 200 μA, exposure time = 3200 ms, filter = 0.5 mm Al, frame averaging = 3, amount of projection images = 1200, isotropic voxel size = 2.8 μm. Projections were reconstructed with Nrecon software (v1.6.9.8) with beam hardening and ring artifact corrections applied. Sample preparation procedure is shown in Fig. 1. The study was carried out under institutionally-approved ethic committee certificates (CÉR-13/14-30 for Polytechnique Montreal and CÉR: 14060 for Maisonneuve-Rosemont Hospital).

Histological grading and quantitative image analysis

After μCT imaging, the sample fixation was continued until 5 days of total fixation was reached. The samples were decalcified in ethylenediaminetetraacetic acid (EDTA) solution for 2 weeks and then embedded in paraffin. Three sections with 3 μm thickness were cut from the samples and stained with Safranin O for OARSI histological grading[1]. Moreover, three 5 μm thick slices with a minimum spacing of 30 μm were cut and stained with Masson trichrome for quantitative histological image analyses (Fig. 2). Histological slices were imaged with an automatic slide scanner (Aperio AT2, Leica Biosystems, Wetzlar, Germany) using 40×
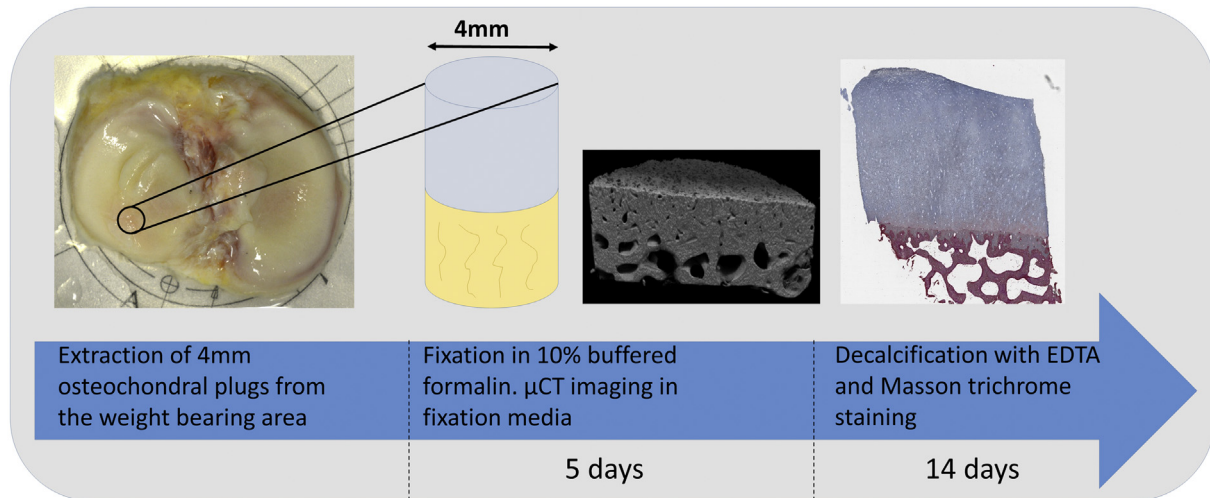
Fig. 1. Preparation and imaging protocol. Osteochondral plugs (Ø = 4 mm) were extracted from the weight bearing area of lateral tibial plateau. Samples were fixed in 10% buffered formalin for 5 days and imaged with μCT after a minimum of 4 days of fixation in fixation media. Subsequently, samples were decalcified in EDTA, embedded into paraffin blocks, sectioned into 5 μm thick slices for Masson's trichrome staining and 3 μm slices for Safranin O staining.
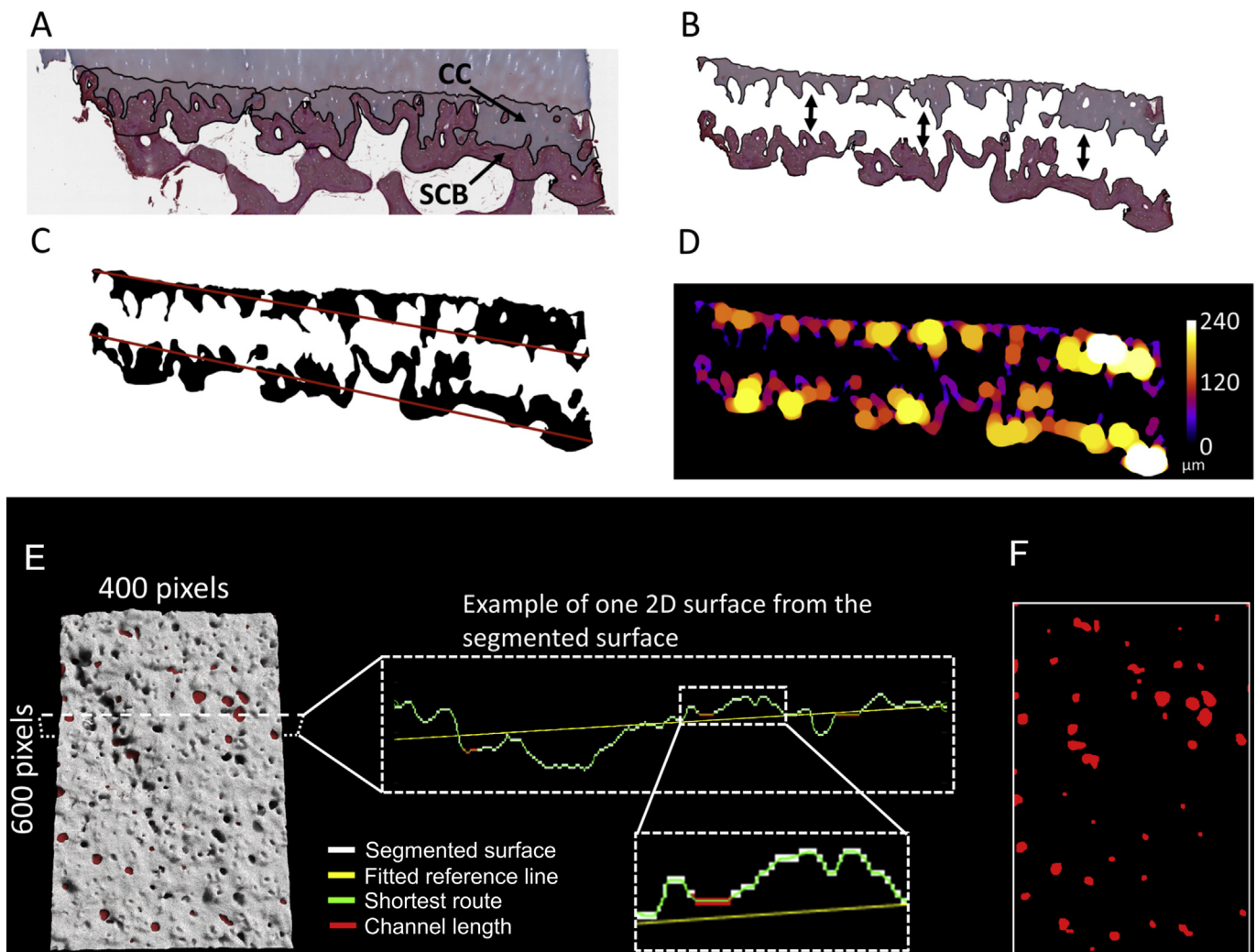
Fig. 2. Histological analyses. A) A Masson trichrome stain from which CC and SCB are manually segmented. B) CC and SCB are separated. C) Mean thicknesses (CC.T_{mean} and SCB.T_{mean}) are calculated by measuring the area of the mask (black) and dividing it by the masks feret diameter (red line). D) Masks from C are used to calculate local thicknesses (CC.T_{local} and SCB.T_{local}). All histological analyses were done on three adjacent slices with a minimum distance of 30 μm between each slice. E) TMR is calculated by measuring the shortest route of 600 segmented 2D surfaces through the stack. A least squares regression line is fitted for each 2D surface and is used as the reference length for each surface. Each samples TMR is the average of these 600 slices. Channel length is removed from each slice if channels are present. Only the surface of the CC is analyzed and not where the channels perforate to the surface. F) Channels that perforate to the surface (red) are used for channel analyses: projection image of the channels from (E).

175

magnification and a 0.25 μm pixel size. The OARSI grading was performed by three individual graders, (SK, SSK, LR) who were blinded to sample quality information during grading. In case of disagreement, a unanimous consensus grade, reached after discussion, was used as the final OARSI grade. Quantitative histological image analyses (Fig. 2) were performed on three slices per sample and average of the three measurements was used as the final parameter. All quantitative histological analyses were done in Fiji[36] using a custom-made macro. First, CC and SCB plate were segmented manually, and masks of the segmentations were used for calculating the cross-sectional areas and feret diameters (longest distance parallel to the joint surface, red line in Fig. 2) as described previously[30]. Local thicknesses of CC and SCB plate were calculated within the macro using BoneJ plug-in[37] as described previously[38]. The calculated parameters were: number of tidemarks (TM.number), CC cross-sectional area per feret diameter (CC.T$_{mean}$), SCB plate cross-sectional area per feret diameter (SCB.T$_{mean}$), local thickness of CC (CC.T$_{local}$), and local thickness of SCB plate (SCB.T$_{local}$) (see Table I for list of parameters).

μCT data analysis

From μCT datasets, volumes of interest (VOIs) were generated with Matlab (v. R2015a, Mathworks, Natick, MA, USA) by fitting a 600 × 400 × Z pixel VOI to the center of the tidemark surface. Z varied between 97 and 330 pixels (271.6–924 μm) depending on the subchondral plate thickness. The calcified content from the VOIs was binarized using fuzzy C-means clustering[39] in a separate custom-made C++ software. The raw data was divided into background and sample with a sample threshold probability of 0.64. C-means convergence was set to 0.0001 which means that iterations stop when the change in probability reaches this value. The continuity of the volume was checked and only the largest object was left as a result. All the subchondral channels were segmented with CTAn software (v1.14.4.1, Bruker microCT, Kontich Belgium) by using ROI-shrink wrap operator in 3D to fit a region of interest to the whole volume. The original volume was then removed from this volume, thus, leaving us with only the channels and some boundary artifacts. Most boundary artifacts were removed using common morphological operations such as closing and opening. Remaining artifacts were removed using despeckle techniques. Subsequently, the binary mask of all the channels within the calcified content was added to the binary mask of the calcified content resulting in a mask where no channels are present. The surface of this combined mask (defining the interface between NCC and CC) was segmented and only the channels in connection with this interface were considered as channels that perforate through bone and CC to the tidemark. As a result, only the channels connecting NCC to the epiphyseal compartment of the tibia were used in the analyses. TMR was calculated as an average roughness from 600 slices from the VOI by finding the shortest route through an automatically segmented surface using an A-star search algorithm (v1.0)[40] and fitting a simple linear regression to each route. The generated regression lines were used as reference lengths for each shortest route through the tidemark surface. If channels were found in any slice, a combined length of these channels was removed from the calculations in order to only analyze the CC surface. Visual explanation of TMR calculation is presented in Fig. 2(E). The equation used to calculate the TMR is:

$$TMR = \frac{1}{n}\sum_{i=1}^{n=600}\left(\frac{shortest\ route_i - channel\ length_i}{reference\ length_i - channel\ length_i}\right) \quad (1)$$

where n = number of slices and i = running slice number. Parameters for the channels were calculated from a projected channel mask and they were: channel area fraction (CAF), channel density (CD), and mean area of the channels (MC.area) [Fig. 2(F)].

A local binary patterns (LBP) -based[41] analysis was conducted for the CC surface to assess the distributions of the local surface orientations in 3D. The same VOIs were used for the LBP-based analysis as for TMR, and the channel mask was used to exclude the locations of the channels perforating to the surface. The LBP-based method used here was adapted from a previous study[42]. Briefly, a specific pattern is calculated for each voxel adjacent to the segmented surface, representing the local volumetric orientation of the surface. Each studied voxel is the center of a sphere with equidistant points fitted on it. A pattern is then calculated by assessing which points are within the surface. Only the patterns that have a clear orientation (uniform patterns) were selected for the analysis. Eventually, a pattern represents the local volumetric orientation of the surface within the neighborhood of the studied voxel. In our analyses, a radius of 2.8 μm was used for the neighborhood distance and 32 points were fitted on each sphere to define the amount of potential different patterns (here two[32]). Amount of different patterns (ADP) gives count of all different local patterns in the sample surface. The higher the ADP, the more different local volumetric orientations are observed within the studied surface. The count was then normalized by the analysis area due to removal of channel locations. To quantify the consistence of each pattern along the sample, the entropy of the patterns distribution (EP) was calculated as follows:

$$EP = -\sum_i P_i \log_2 P \quad (2)$$

P_i contains a count of a specific pattern i. EP describes the randomness of the local patterns, which represents how likely a specific pattern might occur within the sample[42]. The homogeneity index (HI)[42] of local angles was also calculated. This parameter describes the continuity of the angles calculated from the patterns by quantifying the overall local variations in orientations along the surface. An angles co-occurrence matrix –based approach is used to assess how the orientations of the discrete areas of the surface differ from their local surroundings. The method is described in detail in Thevenot *et al.* (2017)[42].

Statistical analyses

Linear associations between the parameters were evaluated using Pearson's correlation coefficient, r_p, for continuous variables and Spearman's rho, r_s, if either of the tested variables were ordinal. Correlation coefficients of 0.40–0.59 were considered as moderate, 0.60–0.79 as strong, and above 0.80 as very strong[43]. Samples were also divided into three groups based on the OARSI grading (healthy (OARSI = 0, $n = 5$), early OA (OARSI = 1–2, $n = 7$) and advanced OA (OARSI >2, $n = 3$)) in order to see if changes in CC can be seen in the earliest stages of OA, where there are minimal changes in the superficial layer of cartilage. Differences between the OARSI groups were tested using a linear mixed model which takes correlation between the tibias of the same subject into account. OARSI grade was set as a fixed and the subject as a random variable. Restricted maximum likelihood estimation was used in the model. A *P*-value smaller than 0.05 was considered statistically significant. Statistical analyses were performed using SPSS (v. 22.0, IBM SPSS, Armonk, NY, USA).

Table I
List of parameters

Parameters	Description	Definition
TMR	Tidemark roughness	Ratio of segmented tidemark length along the surface vs a least square sum fitted line length [Equation (1)][31].
ADP	Amount of different patterns per average analysis area	Sum of different pattern identifiers within a considered area, each studied voxel has a pattern based on the local orientation of the calcified cartilage surface within a defined radius[42].
EP	Entropy of pattern distribution. Describes the randomness of the pattern distribution	Low entropy value corresponds to a uniform volumetric orientation of the surface while a high entropy corresponds to a surface with more local deviations [Equation (2)][42].
HI	Homogeneity index	HI is a value between 0 and 1. A high HI corresponds to a smooth surface locally while a low HI is representative of sharp local deviations on the surface continuity.
CAF	Channel area fraction	A ratio of total channel area perforating to the surface of calcified cartilage vs the analysis area.
CD	Channel density [$1/mm^2$]	Number of separate channel openings per mm^2.
MC.area	Mean channel area [pixels]	Total channel area divided by the number of separate channels perforating to the surface of calcified cartilage in number of pixels.
CC.T$_{mean}$	Calcified cartilage cross-sectional area as a measurement of average thickness from histological sections [μm]	Manually segmented calcified cartilage cross-sectional area divided by its feret diameter[30]. Average values were calculated from three slices spaced at a minimum of 30 μm.
SCB.T$_{mean}$	SCB plate cross-sectional area as a measurement of average thickness from histological sections [μm]	Manually segmented SCB plate cross-sectional area divided by its feret diameter[30]. Average values were calculated from three slices spaced at a minimum of 30 μm.
CC.T$_{local}$	Calcified cartilage local thickness from histological sections [μm]	Local thickness of manually segmented calcified cartilage was calculated using Bonej plug-in[38]. Average values were calculated from three slices spaced at a minimum of 30 μm.
SCB.T$_{local}$	SCB plate local thickness from histological sections [μm]	Local thickness of manually segmented SCB plate calculated using Bonej[38]. Average values were calculated from three slices spaced at a minimum of 30 μm.
TM.number	Number of tidemarks from histological sections	Maximum amount of separate tidemarks. Average values were calculated from three slices spaced at a minimum of 30 μm.

Results

The OARSI grade correlated moderately or strongly with EP ($r_s = -0.648$, $P = 0.009$), ADP ($r_s = -0.600$, $P = 0.018$), HI ($r_s = 0.555$, $P = 0.032$) and TMR ($r_s = -0.579$, $P = 0.024$) and with CC.T$_{mean}$ ($r_s = -0.637$, $P = 0.011$) (Table II).

Compared to healthy samples, early OA had lower values of EP ($P = 0.005$), ADP ($P = 0.012$) and TMR ($P = 0.037$), and advanced OA had lower values in EP ($P = 0.014$). No statistically significant differences were found between healthy and advanced OA in ADP ($P = 0.064$) and TMR ($P = 0.142$), or between healthy and early OA, or advanced OA in HI ($P = 0.102$ and $P = 0.055$, respectively). Early OA and advanced OA did not differ in any of the test parameters. Box plots visualizing the group comparisons are shown in Fig. 3.

The channel parameters CAF and CD correlated strongly with ADP ($r_p = 0.876$, $P < 0.0001$ and $r_p = 0.680$ $P = 0.011$, respectively) (Table II). Similar relation was seen between the channel parameters CAF and CD with EP ($r_p = 0.665$, $P = 0.007$ and $r_p = 0.583$, $P = 0.023$, respectively). CAF and MC.area correlated with TMR ($r_p = 0.926$, $P < 0.0001$ and $r_p = 0.574$, $P = 0.025$, respectively). All correlations between OSCC parameters and CC surface parameters are presented in Table II.

TM.number correlated with SCB.T$_{mean}$, CC.T$_{local}$ and SCB.T$_{local}$ ($r_p = -0.806$, $P < 0.0001$; $r_p = 0.553$, $P = 0.033$ and $r_p = -0.684$, $P = 0.005$, respectively) (Table III). TMR, ADP and CAF correlated with CC.T$_{mean}$ ($r_p = 0.699$, $P = 0.004$; $r_p = 0.554$, $P = 0.032$ and $r_p = 0.683$, $P = 0.005$, respectively) (Table III). CD correlated with SCB.T$_{mean}$ ($r_s = 0.534$, $P = 0.040$) and TM.number ($r_p = -0.728$, $P = 0.002$). MC.area correlated with SCB.T$_{local}$ ($r_p = -0.559$, $P = 0.030$) (Table III).

All the measured parameters and their standard deviations (SDs) in the three OARSI groups are presented in Table IV. Feret diameters that were used for normalizing the average thickness measurements, had a coefficient of variation (CV) of 8.14% for CC measurements and 8.29% for SCB measurements in the whole data set. Healthy, early and advanced groups of OARSI had a CV of 4.67%, 8.49% and 9.90% for CC measurements and 4.79%, 9.51% and 9.73% for SCB measurements, respectively.

Discussion

In this study, we established a new method to quantitatively evaluate the roughness, the local surface variations of the tidemark and perforations through CC in 3D. Furthermore, we demonstrated that the established parameters from the tidemark and CC could be used to quantitatively study relationships between pathological features relevant to OA by comparing the parameters with the histological OARSI grade (a measure for OA progression).

While we had samples from two asymptomatic cadavers, only the 26-year-olds samples were classified as healthy (OARSI grades:

Table II
Correlations between OARSI and μCT surface parameters and histology parameter, and between μCT channel parameters and μCT surface parameters. 95% confidence intervals are shown in brackets next to correlation coefficients

	μCT surface parameters			Histology	
	TMR	ADP	EP	HI	CC.T$_{mean}$
OARSI	**−0.579** (−0.84, −0.10)*	**−0.600** (−0.85, −0.13)*	**−0.648** (−0.87, −0.20)**	**0.555** (0.06, 0.83)*	**−0.637** (−0.87, −0.19)*
μCT channel parameters					
CAF	**0.926** (0.79, 0.98)***	**0.876** (0.66, 0.96)***	**0.665** (0.23, 0.88)**	**−0.254** (−0.68, 0.30)	
CD	**0.477** (−0.05, 0.80)	**0.680** (0.26, 0.88)**	**0.583** (0.10, 0.84)*	**−0.334** (−0.72, 0.22)	
MC.area	**0.574** (0.09, 0.84)*	**0.511** (−0.01 0.81)	**0.341** (−0.21, 0.73)	**−0.186** (−0.64, 0.36)	

***$P < 0.001$, **$P < 0.01$, *$P < 0.05$.
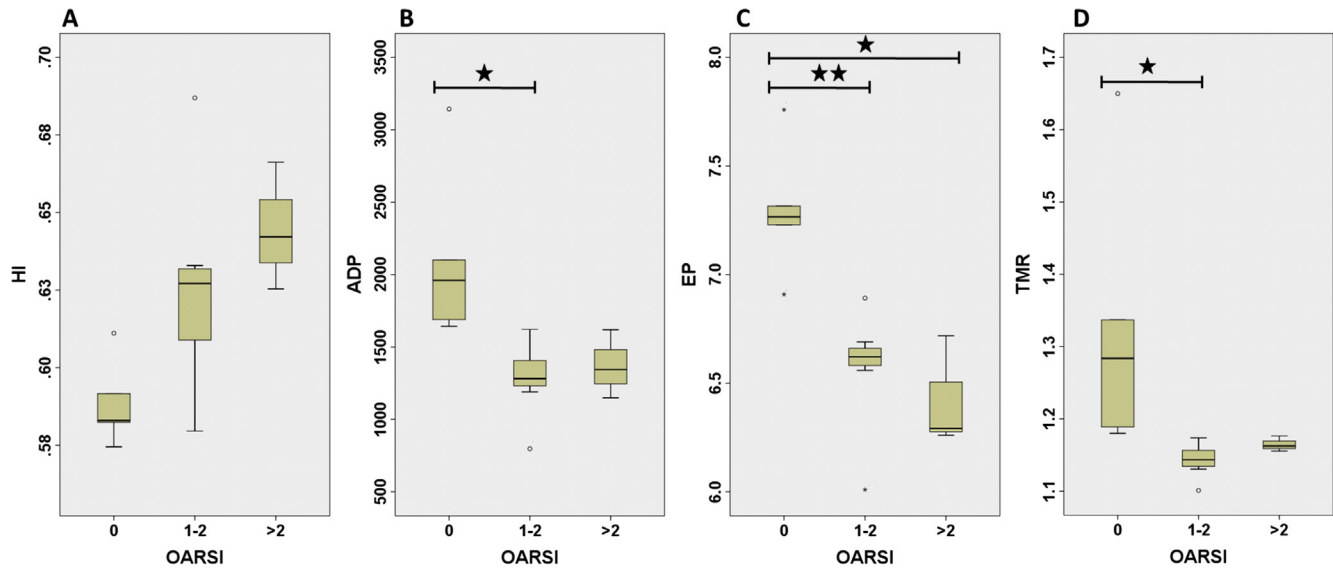
Fig. 3. Box plots of parameters defining surface morphology vs three OARSI groups: healthy (OARSI grade = 0, n = 5), early OA (OARSI grade = 1—2, n = 7) and advanced OA (OARSI grade > 2, n = 3). A) HI, B) ADP, C) EP, D) TMR. Black stars indicate statistical significance (*P < 0.05 and **P < 0.01) between groups.

Table III
Correlations between μCT parameters and histology parameters. Lower and upper 95% confidence levels are shown in brackets next to correlation coefficients

	Histology				
	$CC.T_{mean}$	$SCB.T_{mean}$	$CC.T_{local}$	$SCB.T_{local}$	TM.number
Histology					
TM.number	**0.272** (−0.28, 0.69)	**−0.806** (−0.93, −0.50)***	**0.553** (0.06, 0.83)*	**−0.684** (−0.89, −0.27)**	
μCT surface parameters					
TMR	**0.699** (0.29, 0.89)**	**−0.172** (−0.63, 0.37)	**0.464** (−0.06, 0.79)	**−0.340** (−0.73, 0.21)	**−0.136** (−0.61, 0.40)
ADP	**0.554** (0.06, 0.83)*	**0.049** (−0.46, 0.55)	**0.210** (−0.34, 0.65)	**−0.216** (−0.66, 0.33)	**−0.335** (−0.72, 0.21)
EP	**0.487** (−0.03, 0.80)	**0.085** (−0.45, 0.57)	**0.089** (−0.44, 0.58)	**−0.176** (−0.63, 0.37)	**−0.382** (−0.75, 0.16)
HI	**−0.242** (−0.67, 0.31)	**−0.214** (−0.65, 0.33)	**0.159** (−0.38, 0.62)	**0.024** (−0.49, 0.53)	**0.405** (−0.14, 0.76)
μCT channel parameters					
CAF	**0.683** (0.26, 0.86)**	**−0.135** (−0.60, 0.41)	**0.455** (−0.07, 0.78)	**−0.361** (0.74, 0.19)	**−0.067** (−0.56, 0.46)
CD	**0.052** (−0.47, 0.55)	**0.534** (0.03, 0.82)*	**−0.292** (−0.70, 0.26)	**0.342** (−0.21, 0.73)	**−0.728** (−0.90, −0.35)**
MC.area	**0.476** (−0.05, 0.79)	**−0.345** (−0.73, 0.20)	**0.343** (−0.21, 0.73)	**−0.559** (−0.83, −0.07)*	**0.326** (−0.22, 0.72)

***P < 0.001, **P < 0.01, *P < 0.05.

0 and 0) and the other cadaver (49-year-old) was classified as early OA (grades: 1.0 and 1.5). Three other healthy samples came from TKR patients (two samples from a 49-year-old and one sample from a 56-year-old). On average, the healthy group consisted of the youngest samples in the sample set.

Our results demonstrate association between TMR and OA severity. An OA-related decrease in CC surface roughness was statistically significant in all the parameters describing CC topography. LBP-based parameters (ADP and EP) correlated stronger than TMR with OARSI. Conventional TMR analysis is done slice by slice in 2D. Therefore, complex structures in the surface might not be included in the 2D method. While the LBP-parameters are non-standard measurements, we decided to include them in this study to have a local 3D structural orientation assessment along the sample surface. The real 3D approach includes complex structures, which could explain the differences in the strength of the correlation. Furthermore, the direct relation between HI and OARSI grade was observed. An increase in HI indicates that the studied surface is in overall smoother with less local variations along the surface discrete curvatures. This suggests that, in the current sample set, the surface irregularities in the tidemark diminish with OA progression. Grouping of the samples into three groups of OARSI also revealed that changes of CC topography especially in early OA can

be captured with this method, providing tools for understanding the pathophysiology of OA.

The behavior of roughness of the tidemark during OA could be dominated by small dimples of normal chondrocyte lacunae in healthy cartilage. Especially in healthy samples, chondrocyte lacunae can be seen from our 3D μCT reconstructions [Fig. 4(A)], similarly as in previous SEM studies[27]. The loss of normal chondrocyte function could lead to increased calcification and entrapment of chondrocytes inside CC[44], thus leading to smoothing of the tidemark. To simplify, there could be two kind of roughness components in the tidemark: "high frequency" roughness, which originates from the chondrocyte lacunae and calcification inhibitory components; and "low frequency" roughness where the more overall form of the tidemark starts to appear as a wavy/undulating shape [Fig. 4(A)] which could lead to an increase in low resolution roughness measurements as can be seen in the work by Deng et al. (2016)[30]. Combined findings from these studies would lead to a decrease-increase-decrease response of the TMR in OA. First, the high frequency roughness disappears (entrapment of the chondrocytes), then the low frequency undulations start to appear (uneven increase in calcification) and in the end (after the cartilage is eroded), the tidemark is completely smoothed by physical force of the bones grinding together.

Table IV
Mean and SD from the measured parameters in the three OA groups

|	OARSI		
	0 ($n = 5$)	1—2 ($n = 7$)	>2 ($n = 3$)
	Mean (SD)	Mean (SD)	Mean (SD)
μCT surface parameters			
EP	7.30 (0.30)	6.57 (0.27)	6.42 (0.26)
ADP	2107.55 (609.30)	1287.80 (258.70)	1370.85 (236.53)
TMR	1.33 (0.19)	1.14 (0.02)	1.16 (0.01)
HI	0.59 (0.01)	0.63 (0.03)	0.65 (0.02)
μCT channel parameters			
CAF [%]	8.42 (7.57)	2.24 (1.93)	5.86 (0.85)
CD [/mm^2]	19.56 (7.52)	11.01 (7.71)	14.35 (9.45)
MC.area [pixel count]	568.06 (387.80)	236.05 (216.13)	667.68 (383.47)
Histology parameters			
CC.T$_{mean}$ [μm]	236.84 (97.93)	166.94 (42.56)	142.06 (27.70)
SCB.T$_{mean}$ [μm]	250.68 (58.46)	278.14 (99.25)	246.23 (154.68)
CC.T$_{local}$ [μm]	176.52 (51.31)	161.21 (44.83)	155.50 (25.92)
SCB.T$_{local}$ [μm]	161.60 (47.26)	194.13 (38.12)	176.03 (69.63)
TM.number	1.80 (0.84)	2.62 (1.33)	2.88 (2.46)
OARSI grade	0.00 (0.00)	1.57 (0.45)	4.17 (0.29)
Feret diameter CC [μm]	3865.09 (180.50)	3746.61 (318.22)	3533.09 (349.75)
Feret diameter SCB [μm]	3837.35 (183.58)	3726.88 (354.43)	3626.31 (352,99)
Age	41.20 (14.17)	53.43 (4.47)	64.33 (2.31)

When comparing our results with the literature, similar results with TMR have been reported in histomorphometric analyses of rat CC in a post-traumatic OA model[31]. This previous study found that the TMR decreased in tibial plateaus of rats with increasing OA progression (Mankin et al.[45] score). In contrast, histomorphometric analyses of TMR have shown contradicting results with human samples[30], as roughness was seen to increase with OA progression (e.g., OARSI grade). The same roughness parameter was used in these previous studies, but they did not present the resolution of the acquired images. As the resolution determines the minimum size of the measurable feature in the surface, the results might not be fully comparable.

We found no statistically significant association between the OARSI grade and OSCC area fraction, density or average size. However, there was a strong correlation between the OSCC parameters and the surface parameters (Table II). For the first time, these results demonstrate a relationship between the tidemark surface irregularities and the perforations through the subchondral plate. This indicates an increase in TMR — also in local variations — when more OSCC perforations are present. This warrants for further investigation of this matter using a larger sample size.

OARSI grade showed an indirect relationship with CC.T$_{mean}$. This relation can be explained by the location of the samples as there is a thicker CC in load bearing areas and healthy samples have a thicker CC. However, this would mean that the SCB replaces the CC as OA progresses and a direct relation between OARSI and SCB.T$_{mean}$ would be expected but this relation was not seen in either thickness measurements of the SCB. We saw a positive correlation between CAF and CC.T$_{mean}$. As we are using the samples from the load bearing area of the tibial plateau, where CC and SCB are believed to be thicker[46], these results are in line with findings of Lane et al. (1977)[47]. They found that remodeling of the SCB and CC was increased at the load bearing areas of the human femur. Furthermore, they detected a higher number of vessels in the load bearing sites regardless of age of the patient.

Number of tidemarks showed a negative correlation with both thickness measurements from SCB and a positive correlation with CC.T$_{local}$. These results indicate that with a thicker SCB, fewer tidemarks are present and a thicker CC has a greater number of tidemarks than thinner CC. This is in line with Doube et al. (2007)[24], where they found that CC thickness in 18 month old equine distal metacarpal condyle is dominated by chondroclastic resorption (bone replacing CC) rather than advancing of the
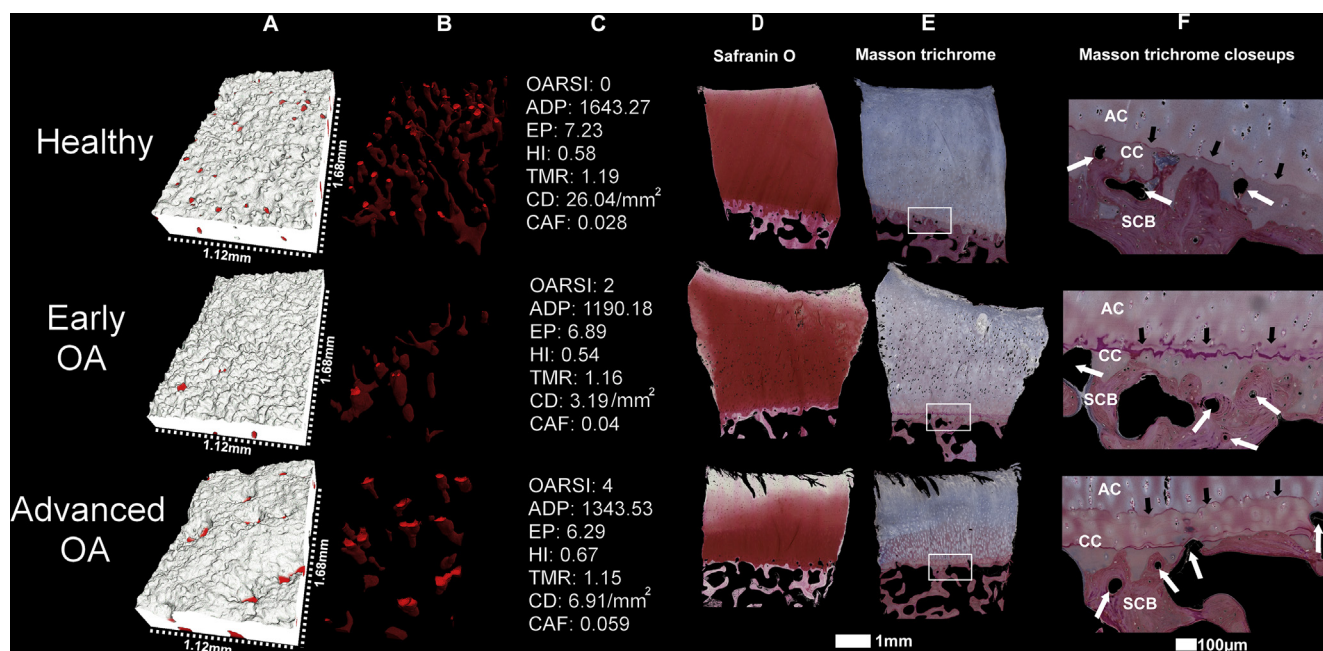
Fig. 4. A panel of three different samples from the study. Healthy, early OA and advanced OA. A) Binarized calcified cartilage surfaces of three volumes used in the analyses. The locations where channels surface can be seen in red. B) volumetric visualization of the channels within the calcified content are seen in red. A brighter shade of red shows where the deep non calcified cartilage is in contact with the medullar area under the subchondral plate. C) corresponding parameters from these samples are shown next to each sample. D) Safranin-O histological staining of the sample. A decrease in red color intensity indicates a proteoglycan loss. E) Masson trichrome histological stain. F) Closeups from the tidemark region from white boxes in (E). Black arrows indicate the location of the tidemark and white arrows show where possible channels are in these sections.

tidemark, which leads to multiple tidemarks[24]. This could potentially mean that SCB plate has replaced enough CC to hide "older" tidemarks in the deep CC as seen in Fig. 4(F), where in advanced OA the bone has replaced the lowest tidemark in the right side of the image. The number of tidemarks was also seen to decrease when the amount of separate OSCCs increase, but no correlation was found when compared to CAF and MC.area. The effect that the OSCCs may play is most likely related to their function (avascular or vascular).

Studying CC surface with μCT is superior to histology as it negates the need of manual segmentation and histological staining, which both can affect the reliability of the results. The segmentation of calcified content from soft tissue from μCT images is relatively easy as the X-ray attenuation between these tissues is so distinctive. Therefore, automatic user independent thresholding, such as fuzzy C-means clustering, is a repeatable and reliable way to segment calcified content from soft tissue. Unfortunately, the cement line (CC-SCB-interface) is indistinguishable with basic desktop μCT. However, with different imaging modalities, such as synchrotron X-ray and phase contrast X-ray imaging, this method could be used for quantifying the cement line topography also[48]. We have no means of separating different types of channels from each other in this study. Limitations in contrast of soft tissue and resolution also make this method incapable of answering the question whether or not blood vessels are present within the detected channels. To differentiate the vascular from avascular channels with μCT, further studies with vessel and soft tissue specific contrast agents would be required.

While the developed methods reveal quantitative associations between the pathological parameters related to CC, the results may or may not be representative for large population. However, OARSI grading focuses mainly on changes in the NCC while our method focuses on changes in CC topography. Decrease in CC surface roughness co-occurs with increasing OARSI grade. This association highlights that changes in CC topography are relevant in the progression of OA. Most importantly, the results demonstrate the feasibility of the developed methods for investigating these associations. In conclusion, we have established a new 3D method for quantifying tidemark topography and perforations through CC. The established methods provide means to study the structure of CC quantitatively from μCT images.

Author contributions
SK, HJN, and SS contributed to the conception and design of the study. SK, HJN, SSK, IK, IH, EQ, MB, MG, and SS. participated in acquisition of the data. SK, SSK, TY, JT, LR, MAF, MH, HJN, and SS participated in analysis of the data. All authors contributed to interpreting the data, drafting or revising the manuscript, and have approved the submitted version of the manuscript.

Competing interests
HJN, TY, and SS are inventors in a patent application related to image analysis of AC. Other authors report no conflicts of interest.

Role of the funding sources
Funding sources are not associated with the scientific contents of the study.

Acknowledgments

Supplementary data

Supplementary data to this article can be found online at https://doi.org/10.1016/j.joca.2018.09.009.

References

1. Pritzker KP, Gay S, Jimenez SA, Ostergaard K, Pelletier JP, Revell PA, *et al.* Osteoarthritis cartilage histopathology: grading and staging. Osteoarthr Cartil 2006;14:13–29. S1063-4584(05)00197-4 [pii].

2. van der Kraan PM, van den Berg WB. Osteophytes: relevance and biology 2007;15:237–44, https://doi.org/10.1016/j.joca.2006.11.006.

3. van der Kraan PM, van den Berg WB. Chondrocyte hypertrophy and osteoarthritis: role in initiation and progression of cartilage degeneration? Osteoarthr Cartil 2012;20:223–32, https://doi.org/10.1016/j.joca.2011.12.003.

4. Chaudhari AM, Briant PL, Bevill SL, Koo S, Andriacchi TP. Knee kinematics, cartilage morphology, and osteoarthritis after ACL injury. Med Sci Sports Exerc 2008;40:215–22, https://doi.org/10.1249/mss.0b013e31815cbb0e.

5. Andriacchi TP, Mundermann A. The role of ambulatory mechanics in the initiation and progression of knee osteoarthritis. Curr Opin Rheumatol 2006;18:514–8, https://doi.org/10.1097/01.bor.0000240365.16842.4e.

6. Vincent KR, Conrad BP, Fregly BJ, Vincent HK. The pathophysiology of osteoarthritis: a mechanical perspective on the knee joint 2012;4:S3–9, https://doi.org/10.1016/j.pmrj.2012.01.020.

7. Hayami T, Pickarski M, Wesolowski GA, McLane J, Bone A, Destefano J, *et al.* The role of subchondral bone remodeling in osteoarthritis: reduction of cartilage degeneration and prevention of osteophyte formation by alendronate in the rat anterior cruciate ligament transection model. Arthritis Rheum 2004;50:1193–206, https://doi.org/10.1002/art.20124.

8. Wen C, Lu WW, Chiu KY. Importance of subchondral bone in the pathogenesis and management of osteoarthritis from bench to bed 2014;2:16–25, https://doi.org/10.1016/j.jot.2013.11.004.

9. Li G, Yin J, Gao J, Cheng TS, Pavlos NJ, Zhang C, *et al.* Subchondral bone in osteoarthritis: insight into risk factors and microstructural changes 2013;15:223, https://doi.org/10.1186/ar4405.

10. Goldring MB, Goldring SR. Articular cartilage and subchondral bone in the pathogenesis of osteoarthritis. Ann N Y Acad Sci 2010;1192:230–7, https://doi.org/10.1111/j.1749-6632.2009.05240.x.

11. Goldring SR. Alterations in periarticular bone and cross talk between subchondral bone and articular cartilage in osteoarthritis. Ther Adv Musculoskelet Dis 2012;4:249–58, https://doi.org/10.1177/1759720X12437353.

12. Mobasheri A, Rayman MP, Gualillo O, Sellam J, van der Kraan P, Fearon U. The role of metabolism in the pathogenesis of osteoarthritis. Nat Rev Rheumatol 2017;13:302–11, https://doi.org/10.1038/nrrheum.2017.50.

13. Wang F, Ying Z, Duan X, Tan H, Yang B, Guo L, *et al.* Histomorphometric analysis of adult articular calcified cartilage zone. J Struct Biol 2009;168:359–65, https://doi.org/10.1016/j.jsb.2009.08.010.

14. Broom ND, Poole CA. A functional-morphological study of the tidemark region of articular cartilage maintained in a non-viable physiological condition. J Anat 1982;135:65–82.

15. Pan J, Zhou X, Li W, Novotny JE, Doty SB, Wang L. In situ measurement of transport between subchondral bone and articular cartilage. J Orthop Res 2009;27:1347–52, https://doi.org/10.1002/jor.20883.

16. Malinin T, Ouellette EA. Articular cartilage nutrition is mediated by subchondral bone: a long-term autograft study in baboons. Osteoarthr Cartil 2000;8:483–91, https://doi.org/10.1053/joca.1999.0324.

17. Fawns HT, Landells JW. Histochemical studies of rheumatic conditions. I. Observations on the fine structures of the matrix of normal bone and cartilage. Ann Rheum Dis 1953;12:105–13.

18. Redler I, Mow VC, Zimny ML, Mansell J. The ultrastructure and biomechanical significance of the tidemark of articular cartilage. Clin Orthop Relat Res 1975;112:357–62.

19. Rees JA, Ali SY. Ultrastructural localisation of alkaline phosphatase activity in osteoarthritic human articular cartilage. Ann Rheum Dis 1988;47:747–53.

20. Anderson HC. Matrix vesicles and calcification. Curr Rheumatol Rep 2003;5:222–6, https://doi.org/10.1007/s11926-003-0071-z.

21. Dziewiatkowski DD, Majznerski LL. Role of proteoglycans in endochondral ossification: inhibition of calcification. Calcif Tissue Int 1985;37:560–4.

22. Luo G, Ducy P, McKee MD, Pinero GJ, Loyer E, Behringer RR, et al. Spontaneous calcification of arteries and cartilage in mice lacking matrix GLA protein. Nature 1997;386:78–81, https://doi.org/10.1038/386078a0.

23. Havelka S, Horn V, Spohrova D, Valouch P. The calcified-noncalcified cartilage interface: the tidemark. Acta Biol Hung 1984;35:271–9.

24. Doube M, Firth EC, Boyde A. Variations in articular calcified cartilage by site and exercise in the 18-month-old equine distal metacarpal condyle. Osteoarthr Cartil 2007;15:1283–92. S1063-4584(07)00130-6 [pii].

25. Dequeker J, Mokassa L, Aerssens J, Boonen S. Bone density and local growth factors in generalized osteoarthritis. Microsc Res Tech 1997;37:358–71, https://doi.org/10.1002/(SICI)1097-0029(19970515)37:4<358::AID-JEMT10>3.0.CO;2-L.

26. Bobacz K, Erlacher L, Smolen J, Soleiman A, Graninger WB. Chondrocyte number and proteoglycan synthesis in the aging and osteoarthritic human articular cartilage. Ann Rheum Dis 2004;63:1618–22. 63/12/1618 [pii].

27. Bullough PG, Jagannath A. The morphology of the calcification front in articular cartilage. Its significance in joint function. J Bone Joint Surg Br 1983;65:72–8.

28. Clark JM. The structure of vascular channels in the subchondral plate. J Anat 1990;171:105–15.

29. Duncan H, Jundt J, Riddle J, Pitchford W, Christopherson T. The tibial subchondral plate. A scanning electron microscopic study 1987;69:1212–20.

30. Deng B, Wang F, Yin L, Chen C, Guo L, Chen H, et al. Quantitative study on morphology of calcified cartilage zone in OARSI 0~4 cartilage from osteoarthritic knees 2016;64:149–54.

31. Schultz M, Molligan J, Schon L, Zhang Z. Pathology of the calcified zone of articular cartilage in post-traumatic osteoarthritis in rat knees. PLoS One 2015;10:e0120949, https://doi.org/10.1371/journal.pone.0120949.

32. Gokhale AM, Drury WJ. A general method for estimation of fracture surface roughness: Part II. Practical considerations 1990;21:1201–7, https://doi.org/10.1007/BF02656539.

33. Suri S, Walsh DA. Osteochondral alterations in osteoarthritis 2012;51:204–11.

34. Shibakawa A, Yudoh K, Masuko-Hongo K, Kato T, Nishioka K, Nakamura H. The role of subchondral bone resorption pits in osteoarthritis: MMP production by cells derived from bone marrow. Osteoarthr Cartil 2005;13:679–87. S1063-4584(05)00106-8 [pii].

35. Walsh DA, McWilliams DF, Turley MJ, Dixon MR, Franses RE, Mapp PI, et al. Angiogenesis and nerve growth factor at the osteochondral junction in rheumatoid arthritis and osteoarthritis. Rheumatology (Oxford) 2010;49:1852–61, https://doi.org/10.1093/rheumatology/keq188.

36. Schindelin J, Arganda-Carreras I, Frise E, Kaynig V, Longair M, Pietzsch T, et al. Fiji: an open-source platform for biological-image analysis. Nat Methods 2012;9:676–82.

37. Doube M, Kłosowski MM, Arganda-Carreras I, Cordelières FP, Dougherty RP, Jackson JS, et al. BoneJ: free and extensible bone image analysis in ImageJ. Bone 2010;47:1076–9, https://doi.org/10.1016/j.bone.2010.08.023.

38. Finnila MAJ, Thevenot J, Aho OM, Tiitu V, Rautiainen J, Kauppinen S, et al. Association between subchondral bone structure and osteoarthritis histopathological grade. J Orthop Res 2017;35:785–92, https://doi.org/10.1002/jor.23312.

39. Cannon RL, Dave JV, Bezdek JC. Efficient implementation of the fuzzy c-means clustering algorithms. IEEE Trans Pattern Anal Mach Intell 1986:248–55, https://doi.org/10.1109/TPAMI.1986.4767778. PAMI-8.

40. Ueland ES, Skjetne R, Dahl AR. Marine Autonomous Exploration Using a Lidar and SLAM 2017, https://doi.org/10.1115/OMAE2017-61880. -:V006T05A029.

41. Ojala T, Pietikainen M, Harwood D. Performance evaluation of texture measures with classification based on Kullback discrimination of distributions. In: Proceedings of 12th International Conference on Pattern Recognition 1994;vol. 1:582–5, https://doi.org/10.1109/ICPR.1994.576366. Jerusalem, Israel.

42. Thevenot J, Hirvasniemi J, Finnilä M, Lehenkari P, Saarakkala S. Volumetric assessment of bone microstructures by a 3D local binary patterns based method: bone changes with osteoarthritis. In: Eskola Hannu, Väisänen Outi, Viik Jari, Hyttinen Jari, Eds. EMBEC & NBC 2017: Joint Conference of the European Medical and Biological Engineering Conference (EMBEC) and the Nordic-Baltic Conference on Biomedical Engineering and Medical Physics (NBC), Tampere, Finland, June 2017. Singapore: Springer Singapore; 2018:900–3.

43. Evans JD. Straightforward Statistics for the Behavioral Sciences. Pacific Grove: Brooks/Cole Pub. Co.; 1996.

44. Jiang J, Leong NL, Mung JC, Hidaka C, Lu HH. Interaction between zonal populations of articular chondrocytes suppresses chondrocyte mineralization and this process is mediated by PTHrP. Osteoarthr Cartil 2008;16:70–82. S1063-4584(07)00193-8 [pii].

45. Mankin HJ, Dorfman H, Lippiello L, Zarins A. Biochemical and metabolic abnormalities in articular cartilage from osteoarthritic human hips. II. Correlation of morphology with biochemical and metabolic data. J Bone Joint Surg Am 1971;53:523–37.

46. Milz S, Putz R. Quantitative morphology of the subchondral plate of the tibial plateau. J Anat 1994;185(Pt 1):103–10.

47. Lane L, Villacin A, G Bullough P. The vascularity and remodelling of subchondral bone and calcified cartilage in adult human femoral and humeral heads. An age and stress related phenomenon. J Bone Joint Surg 1977;59(3):272–8.

48. Ismail EC, Kaabar W, Garrity D, Gundogdu O, Bunk O, Pfeiffer F, et al. X-ray phase contrast imaging of the bone–cartilage interface 2010;68:767–71.